CHAPTER-5

*Beam Absent (cold) EM Simulation and Characterization of RF Interaction Structure of S-Band MILO**

*Part of this work has been published as:

1. **V Nallasamy**, C Narasimhamurthy, Geetha, Sanjay Kumar Gupta, Subrata Kumar Datta , SUM Reddy, and P K Jain, "Electromagnetic Simulation and Experimental Characterization of RF Interaction Structure of an S-Band Magnetically Insulated Line Oscillator", *Journal of Electromagnetic Waves and Applications (JEMWA),* - accepted for publication

5.1. Introduction

The basic configuration of MILO has three major sub-sections, including cathode, slow-wave structure (SWS) as a part of anode, and collector or beam dump. The slow-wave structure (SWS) is otherwise called as RF interaction circuit which is shown in Fig. 5.1. This facilitates the interaction between the axially drifting electrons (the region adjacent to the cathode) and the axially directed slow electromagnetic wave to generate microwaves. The pre-requisite of RF circuit design of MILO is the estimation of fundamental frequency. For a cavity depth of d, the fundamental-mode frequency (f) can be approximately estimated as $f = c/4d$, with c as the velocity of electromagnetic wave in free space. However, there is no exact expression for the accurate estimation of fundamental-mode frequency other than field-analysis or 3D electromagnetic simulation as discussed in Chapter 3. Field-analysis and/or 3D electromagnetic simulation invariably requires verification through cold-test measurements, as the analyses always have some approximations and assumptions. In the present chapter, the design and cold simulation of RF interaction circuit of an S-band MILO has been presented. The design was carried out using analytical formulations and was simulated using 3D electromagnetic code CST Microwave Studio for obtaining the dispersion characteristics for the fundamental-mode operation. The RF interaction structure was fabricated with aluminum material and cold-test measurements were carried out for evaluating the dispersion characteristics.

In the present work, the design of a RF interaction structure comprises periodically spaced cavities formed by placing concentric circular discs with apertures in a smooth waveguide for MILO has been considered, as shown in Fig. 5.1. The rest of the chapter is organized as follows: the development of RF interaction structure through fabrication technique is described in Section 5.2. The resonant perturbation technique is

discussed in Section 5.3. The cold characterization of RF interaction structure of S-band MILO is discussed in section 5.4 and simulated dispersion characteristics and validation by cold test measurement are discussed in Section 5.5. The conclusion is drawn in Section 5.6.

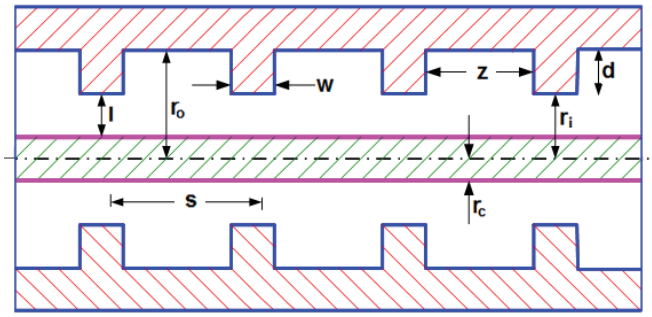

Fig. 5.1: Schematic of RF interaction structures.

5.2. Development of RF Interaction Structure

Using the design parameters presented in Table 3.1, engineering drawings for assembly and piece parts drawings as shown in Fig.5.2 are made using "solid works" modelling software. Further cavity, cathode and end plates of the present RF interaction structure was fabricated using commercial grade Aluminium material. The total length of the cavity structure is 62 mm, the diameter of cavity is 122.8 mm and the cavity wall thickness is 5 mm. A bulk piece of Aluminium material was chosen and in which all four cavities with desired dimensions were machined using PROTECH CNC lathe. The required shape and size of the SWS were machined using tungsten carbide turning tool by holding on a three jaw chuck. The whole cavity structure was machined using specially made tungsten carbide boring tool. Since the length to diameter ratio is higher, thicker boring tool was chosen to avoid chattering resulting in better accuracy. After machining all the machined surfaces were polished using metal wool & lapping pastes. The surfaces are to be burr free and are required to be polished to avoid any electric arcing as the parts used for the high voltage application. It is desirable to

achieve a Roughness surface of Ra 10 micrometer through polishing process. It is important to ensure that the machined surfaces are free from the cutting/lubricant oils which were used during machining. Hence, the RF cavity parts were vapour-degreased using trichloro-ethylene. Then the parts of RF structure were inspected for dimensional accuracy and the surface finish. After inspecting the parts of the RF interaction structure, they have been assembled for cold test measurement as shown in Fig.5.3.

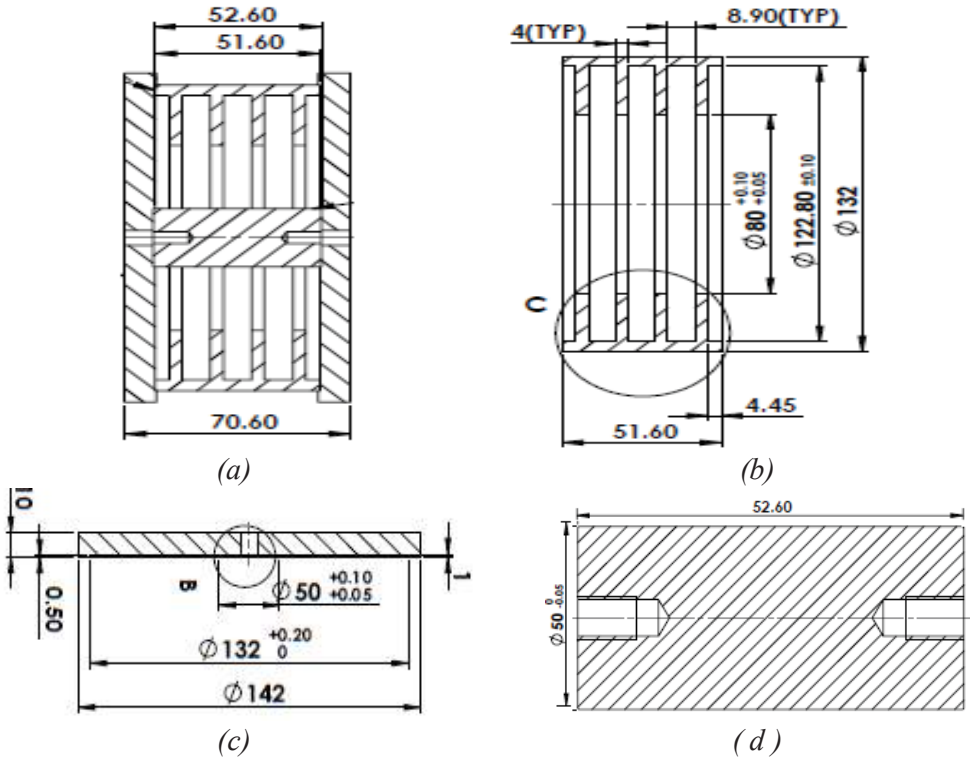

Fig. 5.2 : Assembly and piece parts drawings of RF interaction structure *(a)* Final Assembly of interaction structure *(b)* Cavity *(c)* End plates *(d)* Cathode

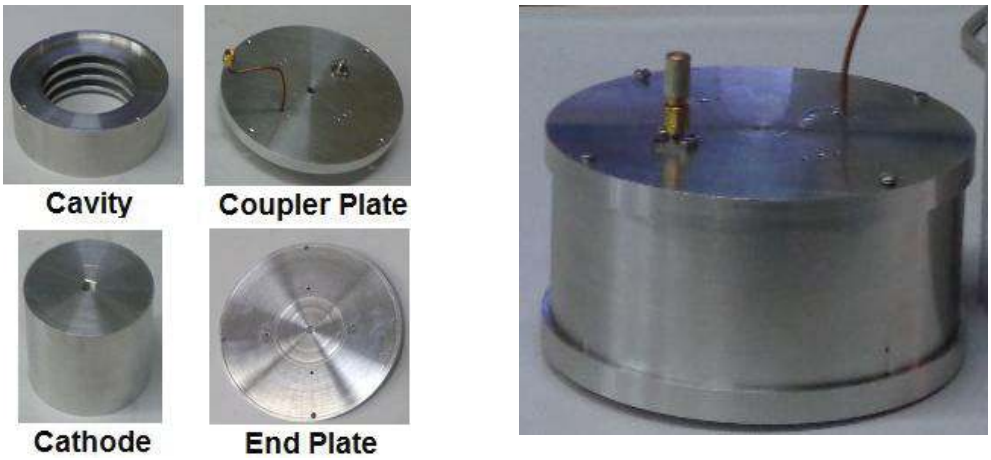

Fig. 5.3: (a) Fabricated piece parts of RF Interaction Structure and (b) Assembly of interaction structure

5.3. Resonant Perturbation Technique

The resonant perturbation technique is the most suitable method for characterization of a periodic RF structure. The resonant perturbation is applicable to periodic structures having planes of mirror symmetry perpendicular to their axes. A resonator has been made out of any periodic structure by placing short-circuiting planes on any two of these planes. The short-circuiting planes have to be placed at the position of electric field in the end cavities, where the planes of mirror symmetry exist. The RF signal has been coupled to the circuit by inserting a loop antenna from the side-wall of the end circuit or by other suitable scheme to couple the dominant mode. The frequencies of resonance have been detected by measuring the return loss profile of the structure, by using a network analyzer. When a small piece of object of magnetic or non-magnetic material or dielectric material is inserted into a resonant cavity ,the resonant frequency is changed by a small amount and the selectivity of the cavity has been reduced. These effects have been generally used in the measurement of the properties of object; the relation between the changes in frequency and selectivity and the properties have been obtained by perturbation theory.

The empty cavity is oscillating in the unperturbed state, in one only of its normal modes. The electric and magnetic fields in the cavity are [Carter, (2001)]

$$\left.\begin{aligned} E &= E_0 e^{j\omega t} \\ H &= H_0 e^{j\omega t} \end{aligned}\right\} \quad , \tag{5.1}$$

where, E_0 and H_0 are functions of position. The field configurations are independent of the field magnitudes, always supposing that in normal working these will not be as large as to cause dielectric breakdown in the cavity or appreciable heating of the walls by induced currents. On inserting a small ferrite or dielectric object into the cavity, the fields and resonance frequency are modified .Thus, we have

$$\left.\begin{aligned} E^{'} &= (E_0 + E_1) e^{j(\omega+\delta\omega)t} \\ H^{'} &= (\mathrm{H}_0 + H_1) e^{j(\omega+\delta w)t} \end{aligned}\right\} \quad , \tag{5.2}$$

The fields in the perturbed case is represented as the sums of the unperturbed fields, E_0 and H_0 and additional fields, E_1 and H_1 with a frequency change δω. It is necessary to mention that $\delta\omega < \omega$ and that over most of the cavity volume E_1 and H_1 are small compared with E_0 and H_0. It is convenient to make these assumptions at the present stage. It is noted that it is not needed that E_1 and H_1 are small when comparing with E_0 and H_0 in the neighbourhood of the object. The E_0 and H_0 in equation (5.2) need not be similar to E_0 and H_0 in equation (5.1). The importance of E_0 and H_0 in equation (5.2) is that they have the same configuration as mentioned in equation (5.1). The E_1 and H_1 are considered as a Fourier sum of all modes except this one, to give the actual field in the cavity. The quantity that has to be measured is the complex frequency shift; this is independent of the amplitudes of oscillation in the perturbed and unperturbed cases, so that, for theoretical purposes, E_0 and H_0 of equation (5.1) are considered as multiplied by some scale factor to make them equal to E_0 and H_0 of equation (5.2). The requirement that E_1 and H_1 are small comparing with E_0 and H_0. This is equivalent to

requiring $\delta\omega$ to be small compared with ω. It is not necessary to stipulate that the energy stored in the sample is small compared with that in the empty cavity, as is sometimes thought. It is sufficient to mention that it is a small fraction of the total energy in the cavity in the perturbed condition. Substituting from equations (5.1) and (5.2) into the Maxwell equation gives

$$\nabla \times E = -\frac{\partial B}{\partial t} \quad , \tag{5.3}$$

We obtain $\nabla \times E_0 = -\frac{\partial B_0}{\partial t} = -j\omega B_0$,

and $\nabla \times (E_0 + E_1) = -j(\omega + \delta\omega)(B_0 + B_1)$,

Subtracting,

$$\nabla \times E_1 = -j[\omega B_1 + \delta\omega(B_0 + B_1)] \quad , \tag{5.4}$$

Similarly,

$$\nabla \times H = \frac{\partial D}{\partial t} \quad , \tag{5.5}$$

We get , $\nabla \times H_1 = j[\omega D_1 + \delta\omega(\mathrm{D}_0 + D_1)]$, (5.6)

Forming the scalar product of H_0 with equation (5.4) and of E_0 with equation (5.6) and adding, we get

$$\begin{aligned} &E_0.\nabla \times H_1 + H_0.\nabla \times E_1 = \\ &j\omega\,[\mathrm{E}_0 D_1 - H_0 B_1)] + \mathrm{j}\,\delta\omega(\mathrm{E}_0 D_0 - H_0 B_0) + (E_0 D_1 - H_0 B_1)] \end{aligned} \quad , \tag{5.7}$$

For outside the object

$$\left.\begin{aligned} B_0 &= \mu_0 H_0 \qquad D_0 = \varepsilon_0 E_0 \\ B_1 &= \mu_0 H_1 \qquad D_1 = \varepsilon_0 E_1 \end{aligned}\right\} \quad , \tag{5.8}$$

and for inside the object

$$D_1 = \varepsilon_0[\varepsilon_r(E_0 + E_1) - E_0] \quad , \tag{5.9}$$

If the object is magnetically isotropic material,

$$B_1 = \mu_0[\mu_r(\mathrm{H}_0 + H_1) - H_0] \quad , \tag{5.10}$$

If the object is gyro-magnetic isotropic material,

$$B_1 = \mu_0\{[\mu_r](\mathrm{H}_0 + H_1) - H_0\} \ . \tag{5.11}$$

Inside the object, ε_r is the relative permittivity or dielectric constant of the object; μ_r is the relative permeability of an isotropic magnetic object, while [μ_r] is the well-known tensor relative permeability of a ferrite. μ_0 and ε_0 are the permeability and permittivity of free space respectively.

By using the vector identity ,it gives

$$Div\,[(H_0 \times E_1) + (E_0 \times H_1)] = \mathrm{E}_1 \cdot curl\, H_0 - H_0 \cdot curl\, E_1 + H_1 \cdot curl\, E_0 - E_0 \cdot curl\, H_1$$

The equations (5.3) and (5.5) can be written as

$$H_0 \cdot curl\, E_1 + E_0 \cdot curl H_1 = j\omega(E_1 \cdot D_0 - H_1 B_0) + div\,[(\mathrm{H}_0 \times E_1) + (\mathrm{E}_0 \times H_1)]$$

Substituting the above equation into left hand side of equation (5.7), we get

$$\begin{aligned} &j\omega(E_1 \cdot D_1 - H_1 \cdot B_0) - div\,[(H_0 \times E_1) + (\mathrm{E}_0 \times H_1)] = \\ &j\omega(E_0 \cdot D_1 - H_0 \cdot B_1) + j\delta\omega[(E_0 \cdot D_0 - H_0 \cdot B_0) + (\mathrm{E}_0 \cdot D_1 - H_0 \cdot B_1)] \end{aligned} \tag{5.12}$$

Let v_0 and v_1 be the volume of the cavity and the volume of the object respectively. Therefore, (v_0 - v_1) is the volume of the object. Integrating equation (5.12) over the volume v_0, we obtain

$$\begin{aligned} &j\omega\iiint_{v_0}(E_1 \cdot D_0 - H_1 \cdot B_0)\,\mathrm{d}v - \iiint_{v_0} div[(H_0 \times E_1) + (\mathrm{E}_0 \times H_1)]\,\mathrm{d}v = \\ &j\omega\iiint_{v_0}(E_0 \cdot D_1 - H_0 \cdot B_1)\,\mathrm{d}v + j\delta\omega\iiint_{v_0}[(E_0 \cdot D_0 - H_0 \cdot B_0) + (\mathrm{E}_0 \cdot D_1 - H_0 \cdot B_1)]\,\mathrm{d}v \end{aligned} \tag{5.13}$$

In the region v_0 - v_1 equation (5.8) has been applied, and the contribution from this region to the first integral on the left-hand side of equation (5.13) is similar to the

first integral on the right hand side. Hence, we only need the contributions to these integrals from the region v_1. For the divergence integral, by using Green's theorem,

$$j\omega\iiint_{V_0} div(H_0 \times E_1 + E_0 \times H_1)dV = j\omega\iint_{S_0}(H_0 \times E_1 + E_0 \times H_1)\cdot\hat{n}dS$$

Where S_0 is the surface of the cavity and n is a unit vector normal to the element dS of S_0 . To the extent to which the cavity walls is considered as perfectly conducting, $H_0 \times E_1$ and $E_0 \times H_1$ are tangential to the walls and their scalar product with $\hat{n}$ is zero. Therefore the divergence integral is vanished. The assumption that $\delta\omega$ is much smaller than ω has been indicated , but no step is taken that depends on this assumption. We now do the first approximation, that depends on the smallness of $\delta\omega$, such as to neglect D_1 and B_1 comparing with D_0 and B_0 in the second integral on the right-hand side of equation (5.13). This has been justified, except in the neighbourhood of the object, by the fact that, when $\delta\omega < \omega$, E_1 and H_1 are small comparing with E_0 and D_0, keeping in mind also the equation (5.8). In the neighbourhood of the object, the contribution to the integral is small, provided that the perturbed fields do not deviate by more than an order of magnitude from the unperturbed values. This approximation becomes the more accurate for smaller v_1 only. when v_1 is smaller, the amount by which the perturbed fields may deviate from their unperturbed values, without reducing the accuracy and equation (5.13) is written as

$$\begin{aligned} j\omega\iiint_{v_1}(E_1\cdot D_0 - H_1\cdot B_0)\,\mathrm{d}v = {} & j\omega\iiint_{v_1}(E_0\cdot D_1 - H_0\cdot B_1)\,\mathrm{d}v \\ & + j\delta\omega\iiint_{v_0}[(E_0\cdot D_0 - H_0\cdot B_0)\,\mathrm{d}v \end{aligned}.$$

Hence, the frequency shift is obtained as

$$\frac{\delta\omega}{\omega} = \frac{\iiint_{v_1}[(E_1 \cdot D_0 - E_0 \cdot D_1) - (H_1 \cdot B_0 - H_0 \cdot B_1)]\,\mathrm{dv}}{\iiint_{v_0}(E_0 \cdot D_0 - H_0 \cdot B_0)\,\mathrm{dv}} \tag{5.14}$$

It is frequently quoted with a plus sign in the denominator. Because, with the definitions of E_0 and H_0 given in the equation (5.1), E_0 and D_0 both contain a phase factor j if the cavity is oscillating in an H mode, or E_0 and B_0 both contain a factor j in the case of an E mode. Thus both $E_0 \cdot D_0$ and $-H_0 \cdot B_0$ have the same sign. Where a plus sign appears in the denominator, the factors j has been removed explicitly. For Non-magnetic object, the second bracket in the numerator of equation (5.14) is zero, hence it becomes,

$$\frac{\delta\omega}{\omega} = \frac{\iiint_{v_1}(E_1 \cdot D_0 - E_0 \cdot D_1)\,\mathrm{dv}}{\iiint_{v_0}(E_0 \cdot D_0 - H_0 \cdot B_0)\,\mathrm{dv}} \quad . \tag{5.15}$$

The only condition required for equation (5.14) and (5.15) to hold is that $\delta\omega/\omega$ should be small. By virtue of equations (5.8), (5.9), (5.10) and (5.11), only the fields have to be considered; the inductions have readily been obtained from the fields . The E_0 and H_0 present no difficulty as they are known for simple shape cavities.

5.4. Cold Characterization of RF Interaction Structure of S-Band MILO

5.4.1. Network Analyzers

A Network Analyzer (NA) is used to cold test any RF resonant or non-resonant structures. This is broadly classified into two categories: Scalar Network Analyzers (SNA) and Vector Network Analyzers (VNA). A vector network analyzer is used for the measurement of Amplitude and phase whereas Scalar Network Analyzer is used for measuring magnitude only. They define the input and output matching of a construction and show how a signal propagates through it. Most analyzers have a capability of simultaneous two-port tests, which means that we do not have to turn the device during the sequence. Components, which we can evaluate, range from coaxial-to-waveguide transitions to power couplers, Ring hybrids and filters. Attenuation is usually expressed in decibels (which is a logarithmic scale), phase shift and group delay are expressed in a linear scale in degrees and time versus frequency, respectively. However, typically the VNA is used in its frequency sweeping mode and impedance or attenuation is shown as a function of frequency. The operating principle relies on a radio transmitter, which changes its frequency. The VNA has also a receiver, which continuously tracks the frequency of the transmitter and we are thus able to plot the performance from one frequency to another. The Smith chart is a very informative impedance display format. Many professionals, too, sometimes prefer to view a logarithmic plot of return loss or standing wave ratio (SWR). For attenuation, phase shift or group delay, conventional rectangular scales are used. Sometimes a polar amplitude plot is practical but its evident drawback is the linear nature. A measurement task usually begins with the calibration of NA. This can be initiated after we have defined the frequency range and the number of measuring samples. The complete two-port calibration is one of the more

accurate procedures. It involves a successive series of opens, shorts and loads followed by a through connection for S_{21}. Naturally we have to use test cables of adequate performance and flexibility. Also, the calibration kit must be of required quality.

There are three main elements to a network analyzer:

1. Power source - may be single frequency (rare), swept source (analogue ramping of frequency) or synthesizer (phase locks at each spot frequency - the most accurate approach).
2. Test set - consists of directional couplers, switches, attenuators, etc., to derive the reference and test signals.
3. Analyzer - compares the reference and test signals and displays the S-parameters as a function of frequency.

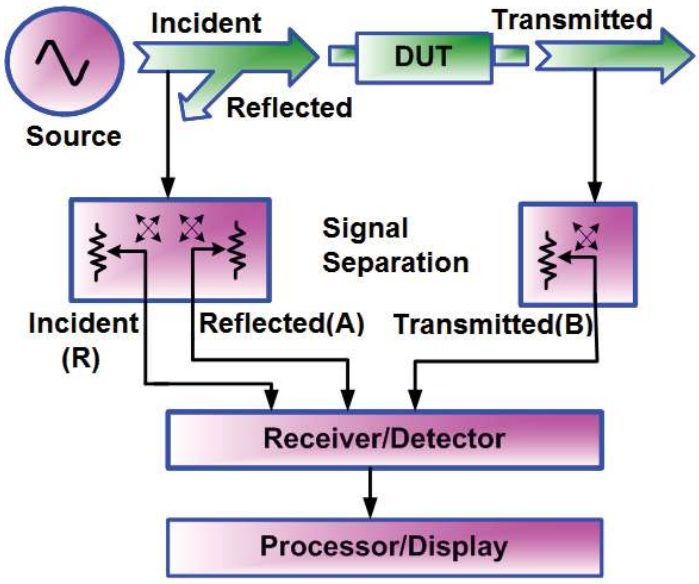

Fig. 5.4: Block Diagram of Scalar Network Analyzer(SNA).

In the present work, a Scalar Network analyzer (SNA) was used for measuring the magnitude of the reflection coefficient. The complete block diagram of the SNA is shown in Fig. 5.4. The SNA usually consists of a source, display/processor and a

transducer. The old version of SNAs rarely had a receiver instead they normally employ wide band diode detectors that have the advantage of being able to make measurements over a very wide frequency range at high speed. Because, this type operates over such a wide range the noise floor usually limits their low amplitude response to around −70 dBm. Diode detectors do not have a linear response to amplitude so the display/processor will also include a table of corrections (within the memory) that are applied to the measured values before being displayed. A very useful application of the scalar network analyzer is its ability to characterize the transmission properties of mixers where the incident signal will be at a different frequency to the output signal. Filters might need to be selected to reject any unwanted signals generated by the mixer.

5.4.2. Measurement Set-up

Figure 5.5 shows the schematic of the present reflection measurement setup that includes a RF source, SNA, directional coupler along with a power divider and the device under test (DUT). The power divider is used to produce the reference channel signal, while the directional coupler measures the reflected wave from the DUT. In the present work, the DUT is shown as a one-port device and the other port is matched terminated for the reflection measurement. The SNA source drives a power divider with one output going to the directional coupler or bridge that inputs the DUT (i.e. SWS), and the other output of the divider connected directly to the reference (R) channel of the analyzer. The output of the DUT is connected to the analyzer (A) channel through directional bridge. The network analyzer is configured to display the DUT response at channel-A divided by the signal present at the reference channel (resulting in an A/R measurement). To the extent that the two channels are matched,

the source flatness is removed from the measurement. When making ratio measurements, the power divider should always be a two-resistor type divider.

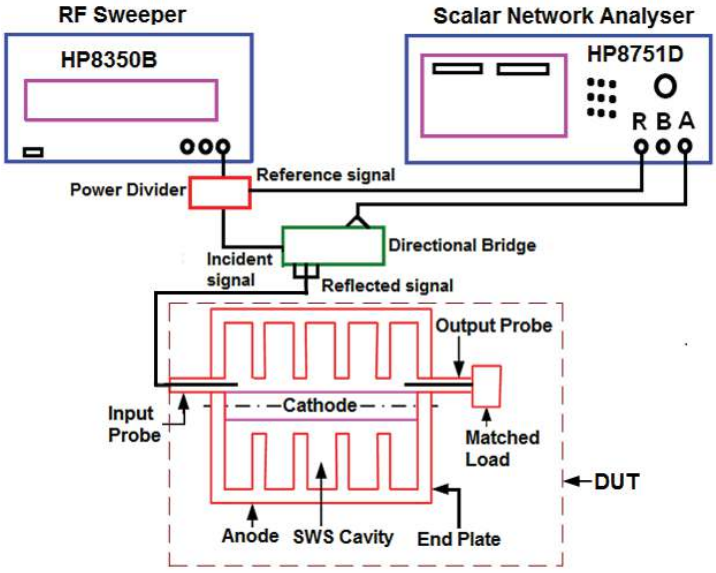

Fig. 5.5: Schematic of cold test measurement set-up includes the DUT (SWS of S-band MILO)

5.4.3. Measurement of Reflection Coefficient

In general, the measurement of scattering parameters of any RF circuit requires the calibration that involves connecting a set of known calibration standards to the appropriate reference plane. The calibration standard is considered as a device that has precisely characterized and well known impedance. The reference plane is the location at which the DUT is connected as shown in Fig. 5.5. Hence, with the calibration standard connected, the SNA measures the relation between the magnitude of the incident and reflected signals along with a well-known impedance of the reference plane. Using these results, the calibration process compensates for internal impairments of the SNA and returns a more accurate measurement result at that reference plane. In practice, the following two types of SNA calibration methods are used to characterize the RF circuit: (i) Short-Open-Load-Through (SOLT), and (ii) Through-Reflect-Line

(TRL). In the present work, the ***SOLT Calibration*** method was used. This is the most popular coaxial calibration method, which involves the process of connecting well-known calibration standards to each port.

After calibrating the ports, the DUT was connected to a signal source and the SNA using SMA-type input and output connectors, respectively on the test bench as shown in Fig. 5.6. The RF signal of 0 dBm was fed to the cavity through one port with the other port of the cavity terminated with a matched load as shown in Fig. 5.6. The return loss profile of the structure was observed from Scalar Network Analyzer as shown in Fig. 5.7**.** It is noted from the cold test measurement that there are 5 resonant frequencies in the return loss profile: 2.4 GHz, 2.505 GHz, 3.06 GHz, 3.558 GHz, and 3.76 GHz.

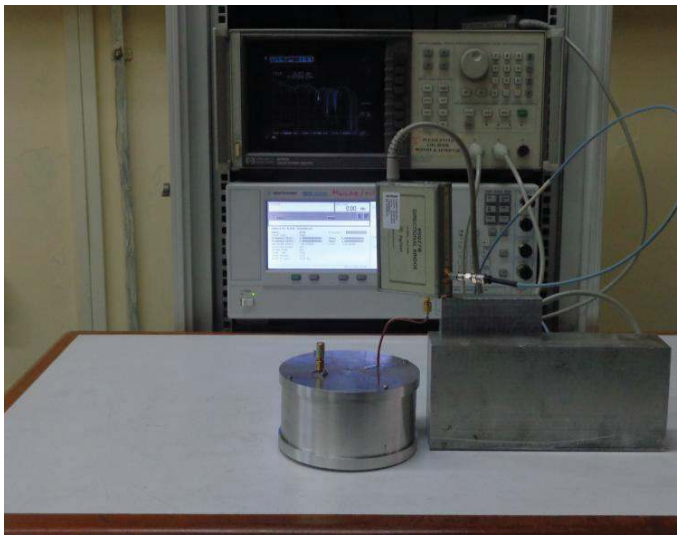

Fig. 5.6: Photograph of DUT connected with Scalar Network Analyzer on test bench.

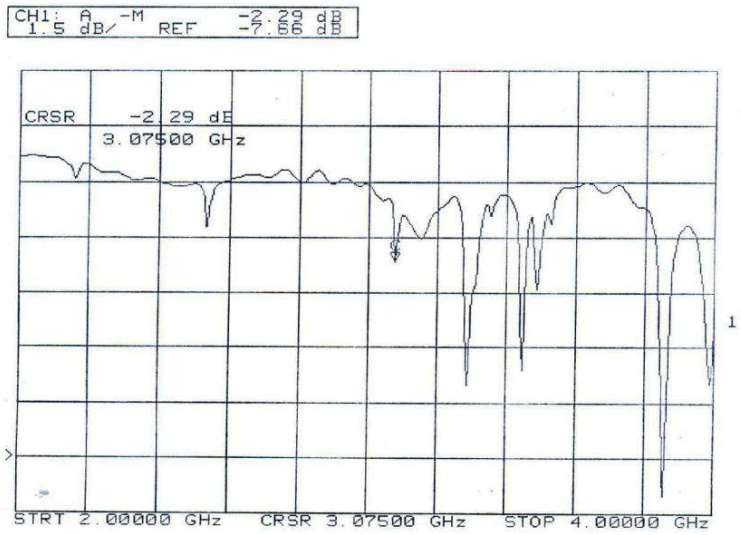

Fig. 5.7: Measured S_{11} performance of the RF interaction structure.

5.5. Simulated Dispersion Characteristics of RF Interaction Structure and Validation by Cold Test Measurement

The SWS of the MILO was modeled to study its cold characteristic using "CST Microwave Studio" as discussed at length in Chapter-3. The simulated 3D model of the RF interaction structure with short-length cathode input and output probes is shown in Fig. 5.8 that includes SWS vanes, cathode, anode, and probes of MILO structure.

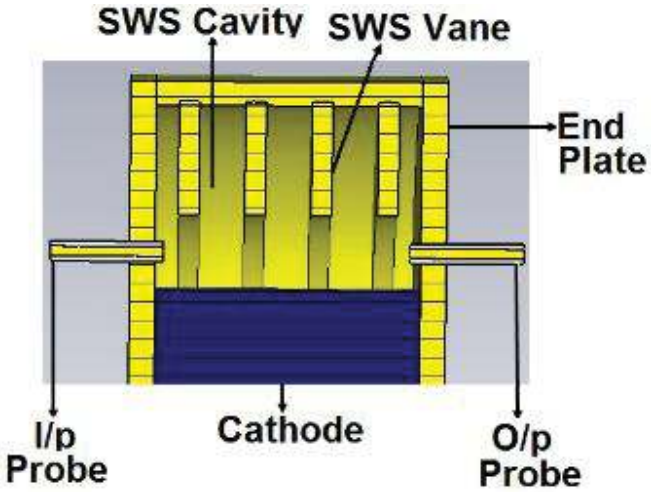

Fig. 5.8: Cut view of the RF interaction structure along with the cathode and the coupling probes

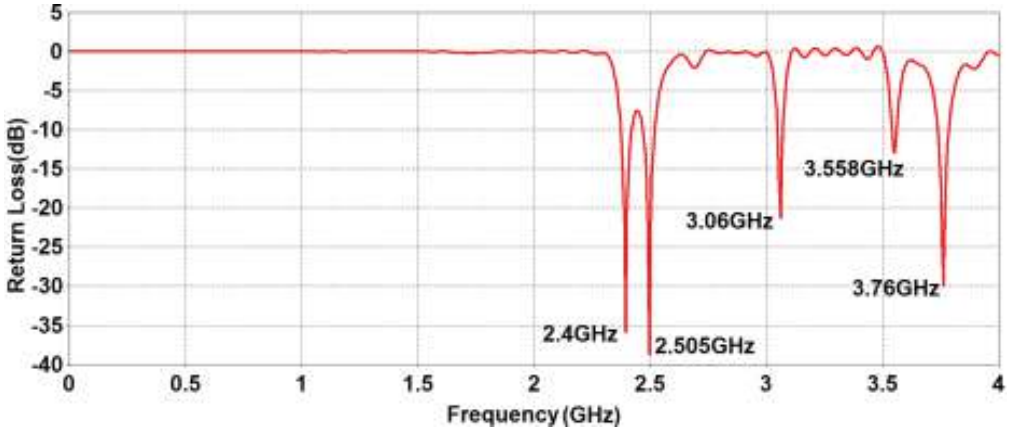

Fig. 5.9: Reflection Coefficient (S_{11}) plot of the RF interaction structure against frequency

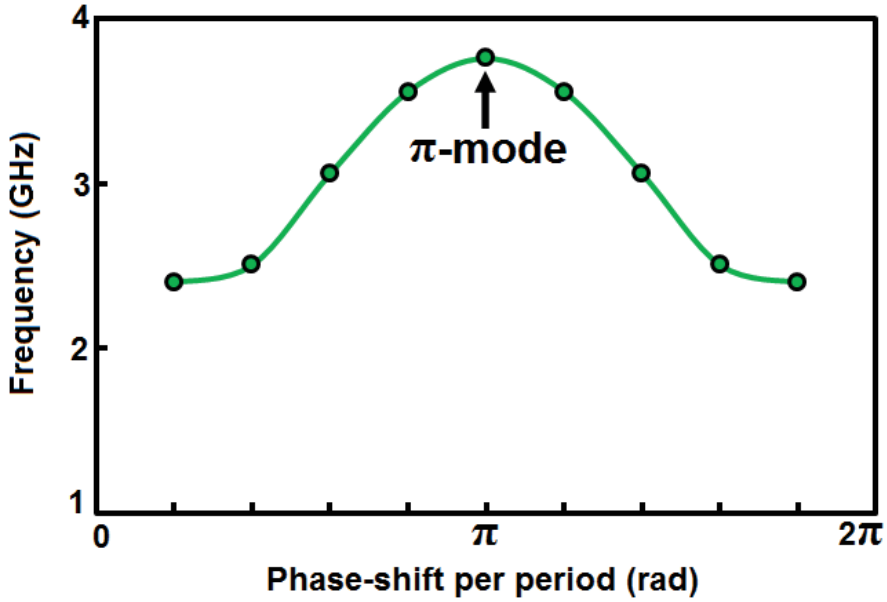

Fig. 5.10 : Simulated dispersion characteristics of the RF interaction structure.

The time domain analysis confirmed the π-mode of operation at 3.7 GHz. The return loss versus frequency and the dispersion characteristics as obtained from the simulation are shown in Figs. 5.9 and 5.10, respectively. These frequencies are interpreted to obtain the dispersion characteristics as compared against simulation in Fig. 5.11. The measured pi-mode frequency was found to be 3.86 GHz against the

simulated value of 3.76 GHz (deviation of around 2.6% with regard to simulation). The shift in π-mode frequency from 3.3 GHz (design frequency) in simulation due to the insertion of probes on both sides of the RF interaction structure. This is due to the fact that insertion of probes causes perturbation of electric field inside the RF interaction structure. The deviation in π-mode frequency during cold test measurements is mainly due to the fabricational tolerances and the corner radius in the experimental cavity along with perturbation of electric field caused by the insertion of probes on both sides of the RF interaction structure.

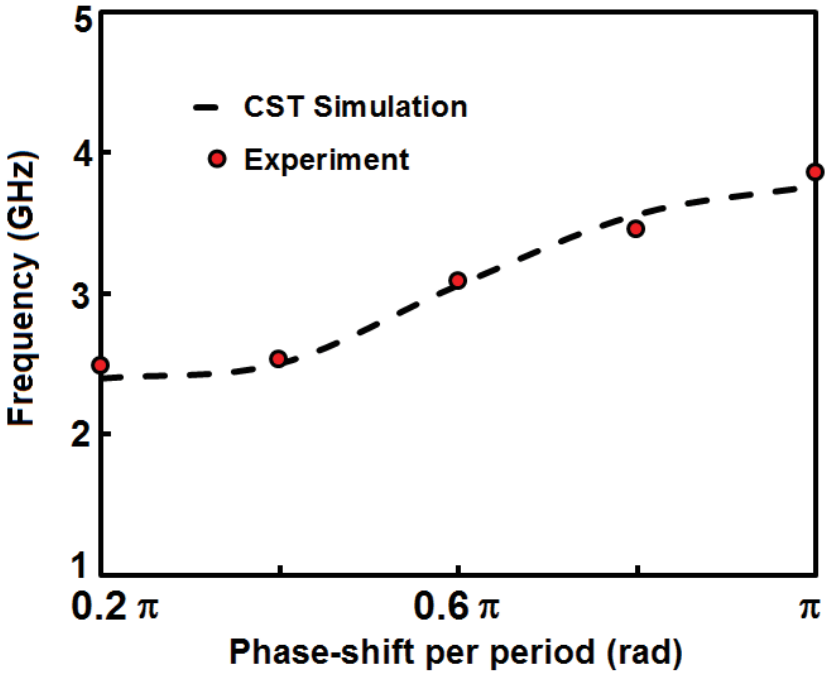

Fig. 5.11: Comparison of simulation and cold-test measurement

5.6. Conclusion

In this chapter, experimental microwave characterization of the developed RF interaction structure of MILO has been carried out. The MILO RF interaction circuit is basically a slow wave structure operating in the TM mode and characterization is made under the electron beam absent (cold) condition using non-resonant perturbation technique. . For this purpose, first the RF interaction structure of S-band MILO has been simulated using CST Microwave Studio under the practical condition, i.e., in presence of an additional metal rod, which has been used here to perturb the electromagnetic field present in the structure. The operating π-mode frequency as per the design discussed in chapter 3 has been validated from the dispersion characteristics obtained from the cold (in absence of the electron beam) simulation and cold test measurements. Based on the design and cold simulation, the assembly and piece parts drawings are made using solid works modelling software and further the piece parts have been fabricated using CNC lathe machine with high precision and accuracy. Later, the piece parts are assembled for cold test measurements using scalar network analyzer (SNA) based on resonant perturbation method. Comparing with the design π-mode frequency (3.3 GHz), the change in cold simulated π-mode frequency is due to the perturbation of electric field by the insertion of probes on both sides of the RF interaction structure. The deviation in measured π-mode frequency against the design and simulated π-mode frequency is mainly due to the fabricational tolerances along with perturbation of electric field caused by the insertion of probes. The measured results are validated against the simulated results of designed operating π-mode frequency. The results obtained from both simulation and measurement have been found in close agreement within 2%, showing the efficacy of the design values of the MILO structure.